

2012 Space Propulsion and Power Program Review
Topic : Plasma/Materials Interactions in Electric Propulsion
Sept. 10-13, 2012, Arlington, VA

“Fundamental Study of Interactions Between High-Density Pulsed Plasmas and Materials for Space Propulsion”

Team:

Laxminarayan Raja, Dept. of Aerospace Engg. and Engg. Mech. (The Univ. of Texas-Austin)

Francesco Stefani, Institute of Advanced Technology (The Univ. of Texas-Austin)

Ian McNab, Institute of Advanced Technology (The Univ. of Texas-Austin)

Graeme Henkelman, Dept. of Chemistry (The Univ. of Texas-Austin)

Roger Bengtson, Dept. of Physics (The Univ. of Texas-Austin)

Waltraud Kriven, Dept. of Materials Sci. and Engg (Univ. of Illinois, Urbana-Champaign)

The aim of the project is the fundamental study of plasma-materials interactions in pulsed, high-pressure, thermal plasmas such as those encountered in a variety of space propulsion devices including Pulsed Plasma Thrusters (PPT), Magneto-Plasma Dynamic (MPD) thrusters and capillary plasma-based thrusters. The ongoing research work brings together a team of researchers from the University of Texas at Austin (UT) and the University of Illinois at Urbana-Champaign (UIUC) with diverse backgrounds in experimental and computational plasma physics, pulsed power engineering, materials science and atomistic-scale materials modeling.

The remaining part of the report discusses a progress made by the respective subgroups working on this project. A summary of the accomplishments for the project as a whole is presented at the end of the report.

Experimental Studies of High-Pressure Capillary Plasma Source (*Stefani, Bengtson @ UT-Austin*)

Our experiments had two specific objectives: 1) to characterize the plasmas produced by our devices to provide accurate inputs to the molecular dynamics (MD) and magneto-hydrodynamics (MHD) simulations, and 2) study plasma-materials interactions. We have sought to produce ablation of order of 10-100 nm in our samples: more ablation than that would make it difficult to tie our experimental results to fundamental theory; less ablation would be difficult to measure with accuracy.

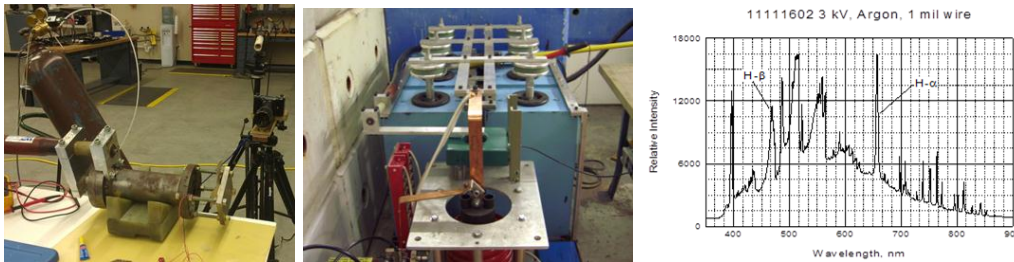


Figure 1: Capillary discharge (left), power supply for the capillary discharge (middle), and a spectrum used to establish plasma temperature and electron density (right).

Our initial experiments were conducted using a large capillary device shown in Figure 1. The device, which was built and characterized in a previous AFOSR program (Award FA9550-05-1-0341), consists of a 23 cm long, hardened AISI 4140 steel chamber into which is inserted a thin, consumable polyethylene liner. The device can generate 5-30 kJ of plasma energy at 1-2 eV, with currents of up to 130 kA, and peak powers of 50-350 MW.

We characterized the plasma from the large capillary at 3 and 4 kV using time-integrated spectroscopy, time-resolved light intensity measurements, and time-resolved pressure measurements at multiple locations.

We estimated the electron density from line broadening of the H β line, and electron temperature from a local thermodynamic equilibrium (LTE) model. From these we calculated the particle flux incident onto the samples. Our results for typical operating conditions are shown in Table 1.

Table 1. Plasma characteristics for tests with large capillary using argon feed gas

Charge Voltage	Peak Current	Peak Power	Plasma Energy	Plasma Pressure At 60 cm	Plasma Temperature	Flux $\Gamma \cdot \tau$	Electron density n_e	Ionization fraction n_e/n
3 kV	13 kA	25 MW	3.5 kJ	0.75 MPa	1 ± 0.3 eV	10^{28} m^{-2}	$5 \times 10^{16} \text{ cm}^{-3}$	0.02
4 kV	18 kA	40 MW	6.3 kJ	0.5 MPa				

The principal finding from our work with the large capillary discharge can be summarized as follows:

- Our test conditions appear to produce little if any ablation on any of the samples, despite the appearance that material has been altered from exposure to the plasma.
- A considerable amount of soot (carbon black) from the consumable hydrocarbon liner deposits onto the samples, presumably during the end of the pulse. This interferes greatly with being able to measure ablation during the main plasma event.

The shortcomings of our ablative capillary device motivated us to redesign our experiment to use a new non-ablative capillary plasma device that can accomodate a controllable feedgas/feedgas mixtures. The new device is required to operate under similar operating conditions as our existing ablative capillary device, i.e. high-pressure operation under pulsed high-power condition to produce a high-density thermal plasma.

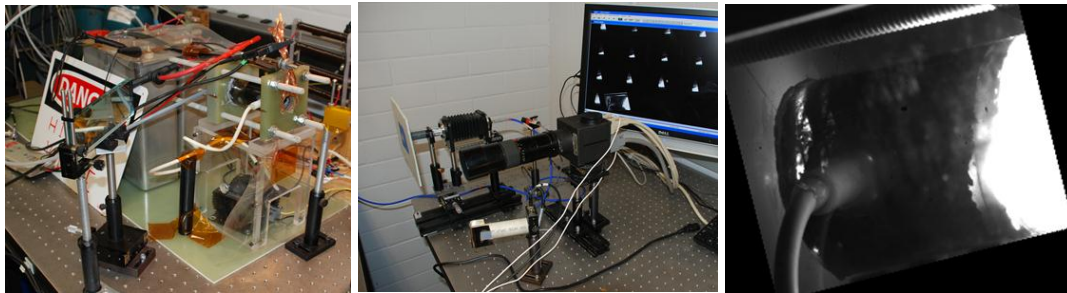


Figure 2: New capillary device that uses a non-consumable liner. Capacitors and capillary (left), high speed camera, spectrometer and photodiode aimed at capillary (center). A frame from a sequence of high-speed images of the plasma in the capillary (right).

The new device is shown in Figure 2 and uses a quartz, non-consumable liner to eliminate condensable material from the plasma. Quartz was selected because it is resistant to thermal shock and allows for optical plasma diagnostics. The new capillary uses a flash lamp approach for triggering to eliminate the need for a consumable fuse wire. In addition to *not* contaminating the plasma with the vaporized fuse wire, this approach has the added benefit of allowing a high throughput of tests, on the order of 50 per hour. Since neither the liner nor the fuse contributes significantly to the plasma, argon is used as the feed gas for our preliminary experiments. Argon thermal plasmas are well understood and the techniques to model and characterize these plasma are well established. The argon is mixed with 2% hydrogen to produce hydrogen lines for plasma spectroscopy.

A new power supply produces shorter and more powerful plasmas than the original device. This is achieved by operating at higher voltages and currents, and with less inductance than in the original design. In its current configuration the power output is greater than 50 MW. With modifications to the power supply we hope to achieve a factor of two to ten increase in power. To compensate for the reduced flux of

argon atoms per exposure, the device has been designed operate at a high repetition rate. This allows us to produce hundreds of exposures per sample, which is what is needed to produce measurable ablation.

Plasma-materials interaction experiments: we exposed samples of 99.5% pure Al_2O_3 , and samples of single crystal silicon (100), some of which are shown in Figure 3. We chose these materials because alumina is commonly used in plasma devices, and single crystal silicon is widely available and has been extensively studied for commercial applications.

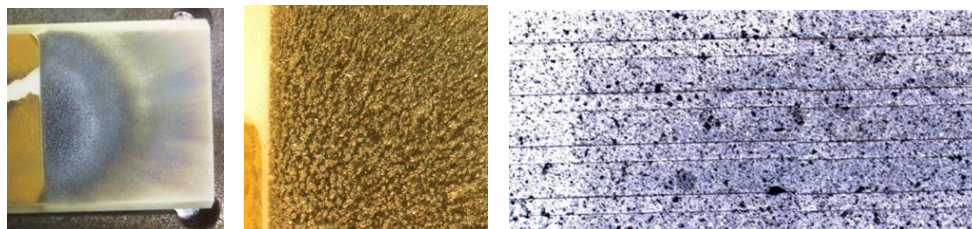


Figure 3: Al_2O_3 tile exposed to plasma (far left), enlarged (center), and exposed (100) silicon (right).

Our tests on 99.5% pure Al_2O_3 consisted of exposing pristine tiles (1" x 2" x 0.5") at a distance of 30 -60 mm from the muzzle of the capillary, oriented normal to the plume. 4-mil thick kapton tape was used as a mask. Microscopic examination of the tiles after exposure by the IAT showed a darkening and texturing of the surface. The tiles were given to the Kriven Materials Group at the University of Illinois for more detailed analysis (reported below).

Tests on single-crystal silicon were similar to those on alumina, and consisted of two series: one in which we exposed as-received samples of silicon; another in which we exposed silicon samples that had been processed in a reactor to produce microscopic channels (trench patterns, which can be seen in Figure 3) to provide reference features for measuring ablation. Using plasma processing equipment at UT we developed techniques for manufacturing and profiling silicon samples for use in this project. Silicon samples were also sent to the Kriven Materials Group at the University of Illinois for detailed analysis.

The findings from the materials tests can be summarized as follows:

- Our test conditions appear to produce little if any ablation on any of the samples, despite the appearance that material has been altered from exposure to the plasma. This finding was suspected by the researcher at UT and confirmed by analyses conducted by the materials scientists at UIUC.
- A considerable amount of soot (carbon black) from the consumable hydrocarbon liner deposits onto the samples. This interferes greatly with being able to measure ablation.

Materials characterization (*Kriven @ UIUC*)

A number of silicon samples were provided by researchers at UT-Austin. Following is a listing of the samples and the plasma exposure conditions as specified by UT-Austin.

Sample	Charge voltage	Distance from muzzle	Number of exposures	Comments
1	4 kV	30mm	2x	Etched micropattern
2	4 kV	30 mm	1x	
3	4 kV	30 mm	2x	
4	4 kV	60 mm	2x	
5	4 kV	60 mm	5x	
6	4 kV	60 mm	2x	
7	4 kV	50 mm	1x	kapton mask
8	n/a	n/a	0	Trench control, not exposed
9	4 kV	60 mm	1x	Trench, exposed

The results of scanning electron microscope (SEM) examinations (Fig. 4) of the silicon samples can be summarized as follows:

1. carbon soot (or carbon black) deposition was evident and abundant,
2. no erosion/ablation of the exposed surface was found except in samples 1, 2 (the common point of these samples was “30 mm”), and 7 (still < 60 mm),
3. even when the surface erosion/ablation was observed in “30 mm” and “50 mm” samples, carbon soot/carbon black deposition was simultaneously present,
4. The most recent “trench-type” sample exposed to plasma showed no erosion/ablation at all, but showed extensive carbon black deposition.

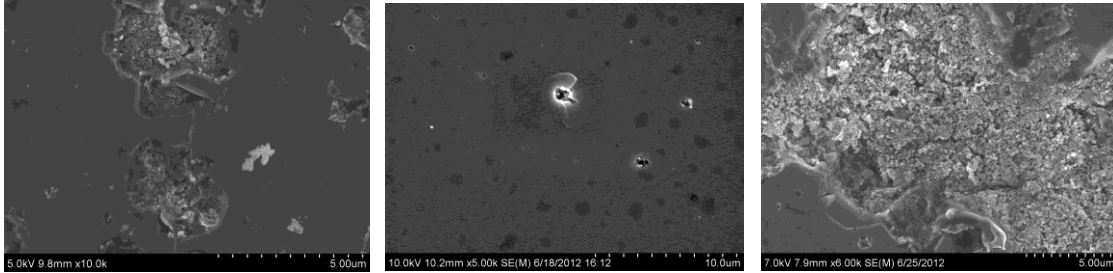


Figure 4: SEM images of samples 1 (left), 2 (center), and 7(right).

Figures 5 and 6 show examination of samples exposed to the original capillary device and confirms the dominant deposition of carbon deposits on the surface.

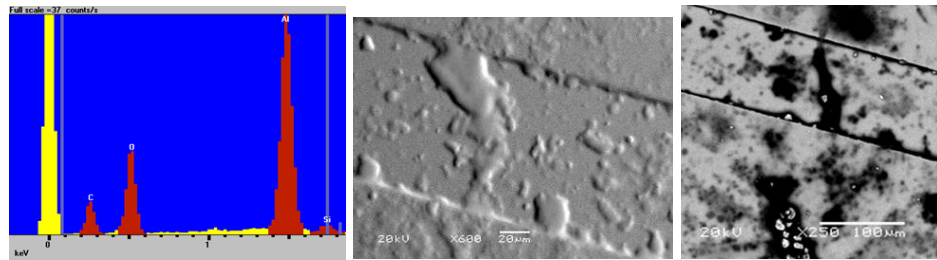


Figure 5: Evidence of contamination by carbon of all exposed samples was confirmed by analyses at UIUC. The figure on left clearly shows a carbon peak (red, labeled “c”) from an SEM-EDXS image of an alumina Al_2O_3 tile exposed to plasma. Figure in the right and on the right are back scattered electron (BSE) images of exposed silicon (center right). Note accumulation of carbon in topographical image (center) and prevalence of black, indicative of carbon on right image.

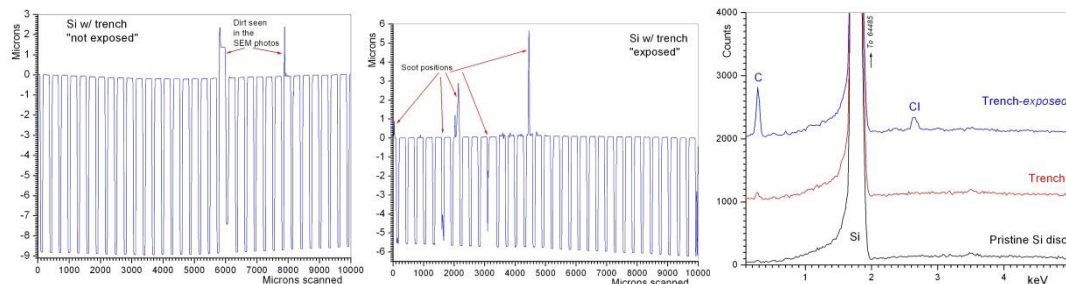


Figure 6: Surface profilometry of samples with trench patterns and EDXS analysis of the samples.

Surface profilometry analyses performed on the silicon samples with trench patterns revealed the extent of carbon black/soot deposition (Fig. 6). EDXS (energy dispersive x-ray spectroscopy) analyses on the latest trench samples confirmed the significant presence of carbon on the plasma exposed silicon sample.

GA-XRD (glancing angle x-ray diffraction) analyses performed by using an angle of incidence of 1° (this angle for Si corresponding to “a depth of penetration by the incident x-rays of the sample surface” of around 2.5 microns) showed that the plasma-exposed surfaces of silicon samples, with the exception of sample-6, was not depicting the characteristic pattern of “poly-Si” (ICDD PDF 27-1402). However, the plasma-exposed surface of sample-6 was found to display the (111), (220), and (311) reflections of “poly-Si” as shown in Fig. 5. The matt sides (unexposed) of all silicon samples were displaying all the XRD reflections of “poly-Si.” The GA-XRD data of the “trench-type Si sample exposed to plasma” and that of “pristine Si disc” are compared to one another in Fig. 7 below, whereas those of matt sides are in Fig. 7.

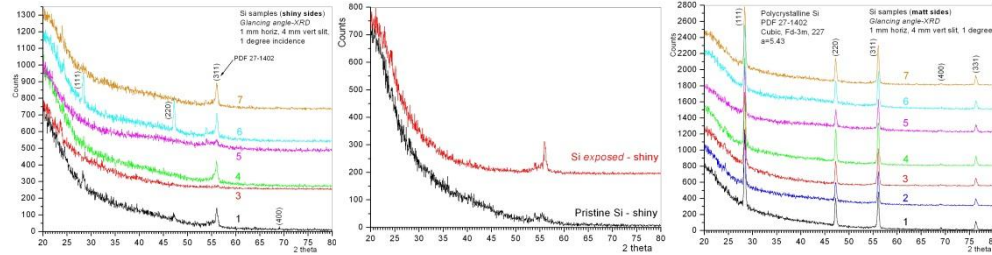


Figure 7 GA-XRD of sample 6 (left), pristine Si disk (center), and matt side of Si sample (right).

The aluminum oxide sample (shown in Fig. 3) (one half of it was exposed to plasma) was too big, which made it impossible to place it into the top-of-the-line electron microscopes without destroying the exposed-unexposed interface line during any ceramic cutting operation. Its dimensions also did not let us to perform non-destructive ATR-FTIR (attenuated total reflection-Fourier transform infrared spectroscopy) analyses on its plasma-exposed surface. EDXS analyses performed on the alumina block showed that it contained silicon as well as carbon (Fig. 5 left). The presence of carbon was due to the carbon black formation in the thermal plasma as described earlier. Silicon oxide is usually encountered in low purity aluminum oxide samples, manufacturers add silicon oxide to alumina processing to form relatively low-melting aluminosilicate phases to enhance densification/sintering at temperatures well below the melting point of Al_2O_3 . High purity alumina ceramics are white in color, the sample we have was unfortunately light beige (or ivory) in color. That off white color of this alumina sample was speaking of its level of impurity at the first glance. The surface profilometry data of the unexposed and exposed portions of that alumina block are given in Fig. 8. The microstructure of the unexposed and exposed alumina sample is shown in Fig. 9. The porous nature of the alumina is evident from this image. The surface profilometry data of Fig. 8 (left) measured the depths of those cavities present on the unexposed-side to be around 8 to 8.5 microns.

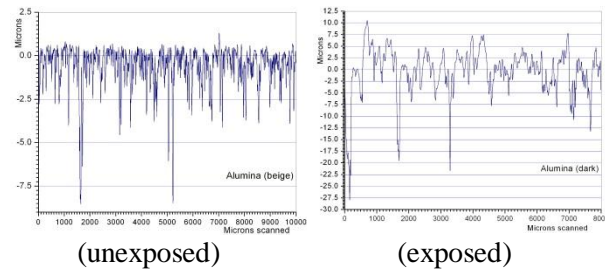


Figure 8: Surface profilometry alumina sample.

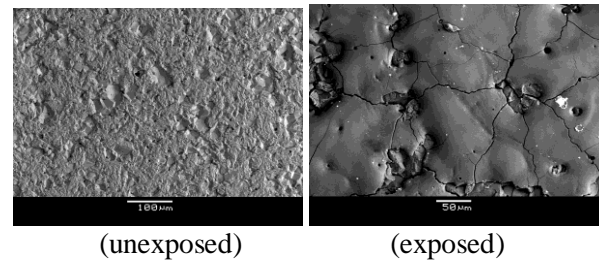


Figure 9: SEM of alumina sample.

The dark substance covering the exposed alumina surface was amorphous to x-rays. This dark substance surprisingly peeled away following 4 minutes of ultrasonification in ethanol.

Computational Modeling of High-Pressure Plasma Source (Raja @ UT-Austin)

Objectives: A magneto-hydrodynamics (MHD) model is developed to characterize the high density plasma in generic electric propulsion devices. The experimental facet of the current project primarily gives spatially averaged measurements of plasma temperature and densities. In order to extent the ability of

determining the particle and energy fluxes more accurately at solid surfaces, the characterization of the plasma with the given experimental conditions is extremely essential. This can be achieved through a high fidelity MHD model. The particle and energy fluxes thus obtained are used as inputs for material models which help in characterizing the ablation rates as well as damage of the surfaces.

MHD governing equations: MHD models have been widely used in studying high density thermal plasmas in electric propulsion and nuclear fusion devices. The MHD equations can be formulated as 8 convection-diffusion equations for the evolution of mass, momentum, energy and induced magnetic fields in a plasma. A finite volume scheme on general mixed unstructured grids is used to solve these equations.

Progress in code development: 1) The time-stepping scheme used during the beginning months of the project was the explicit five stage Runge-Kutta (RK) method. Explicit methods are crippled by stringent time-step constraints in strongly magnetized (small convection time-scales) as well as highly resistive (small magnetic diffusion time-scales) plasmas. In order to overcome this limitation, a semi-implicit time-stepping method has been developed and implemented on general unstructured grids.

2) The code has been extended to function in parallel on multiple compute cores. The semi-implicit method involves a Lower Upper Symmetric Gauss Seidel (LU-SGS) relaxation scheme. This technique primarily involves Gauss-Seidel iterations which has inherent dependencies within itself. Therefore parallelization of this method is not straight-forward. A grid coloring based algorithm is implemented to vectorize these operations. This is the first time that this method is being used to solve the MHD equations on unstructured grids.

Verification cases and parallel performance: A standard MHD shock tube problem has been used as a test case for the numerical discretization of convection term in MHD codes. It is usually studied on a one dimensional domain from 0 to 1. A two dimensional simulation is done here to assess the performance of the code on general unstructured grids. The initial conditions for pressure (P), density (ρ) and magnetic field (B_y) are as shown in Eq. 1. The x component of magnetic field is equal to 0.75.

$$P = \begin{cases} 1.0 & \forall x < 0.5 \\ 0.1 & \forall x \geq 0.5 \end{cases} \quad \rho = \begin{cases} 1.0 & \forall x < 0.5 \\ 0.1 & \forall x \geq 0.5 \end{cases} \quad B_y = \begin{cases} 1.0 & \forall x < 0.5 \\ -1.0 & \forall x \geq 0.5 \end{cases} \quad (1)$$

An unstructured grid consisting of about 16,000 triangular elements were used for this calculation as shown Fig 10 (a). The simulation was done using 8

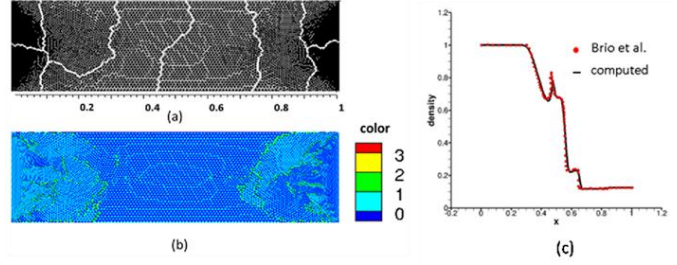


Figure 10: (a) unstructured grid partitioned on 8 processors (b) coloring of the grid (c) solution along axial center line.

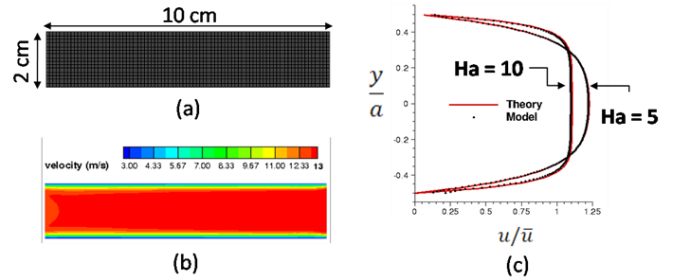


Figure 11: (a) computational mesh (b) axial velocity solution at steady state for Ha = 10 (c) comparison of velocity profile with theory.

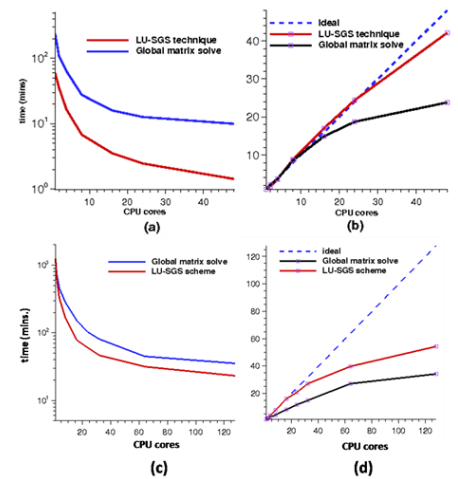


Figure 12: (a) Time in minutes and (b) strong scaling for MHD shock tube test case. (c) Time in minutes and (d) strong scaling for Hartman flow test case.

processors and the domain decomposition. The partition boundaries are indicated in Fig 10 (a). The coloring of the unstructured grid required four colors which is shown in Fig 10 (b). The density solution after time $t=0.1$ extracted along the axial center line is shown in Fig 10(c). The solution agrees well with a benchmark solution in the literature.

To test the non-ideal MHD terms and viscous diffusion terms, the Hartman flow problem is used as verification test case. Hartman flow is essentially the flow of a conducting fluid between two parallel electrodes with a constant applied magnetic field perpendicular to the flow. Figure 11(a) shows the geometry and computational mesh used for the two dimensional planar simulation. The channel is assumed to have a length $l = 10$ cm and width $2a = 2$ cm and the mesh contains 12500 rectangular elements. The pressure at the inflow (left boundary) is fixed at 100 kPa while the downstream end is at 92 kPa. The variation of pressure in the domain is self consistently computed and is linear at steady state. A constant magnetic field ($0.125 \hat{y}$ tesla) is imposed by applying a Dirichlet boundary condition with the same value at all boundaries. The simulation is performed using the time implicit LU-SGS technique. Analytical solution to the problem can be obtained, which depends on the Hartman number (Ha) of the flow. Hartman number is a quantity similar to the flow Reynold's number. It is essentially the ratio of the magnetic Lorentz forces to the viscous forces. . Figure 11(b) shows the axial velocity solution for Hartman number $Ha = 10$. Figure 11(c) shows the axial velocity profile along the cross-section at the middle of the tube. Here \bar{u} represents the average velocity of the profile. The comparison between the theoretical solution and the model is excellent.

Two different methods for the semi-implicit scheme has been used in this study. One of them is the LU-SGS technique which is a matrix free method and the other is where a global matrix is assembled and solved using a minimum residual algorithm. The global matrix assembly and solve is done using the Krylov Subspace (KSP) subroutines in PETSc (Portable Extensible Toolkit for Scientific Computation) libraries. The KSP solver used is GMRES with BJACOBI preconditioning. The matrix free method is less expensive computationally because of lower memory requirements and the absence of global matrix assembly. Figure 12 shows timing and scalability information for both the techniques for the MHD shock tube and the Hartman flow test case. The run times show that the LU-SGS scheme is more efficient compared to the global matrix solve method. The time taken by the global matrix solve was about 10 minutes as opposed to about a minute using the LU-SGS method on 48 processors. The strong scaling curve for the LU-SGS technique shown in Fig 12(b) reveal that the communication and partition boundary calculations start degrading performance only around 48 cores. The global matrix technique scales well until 24 cores. Figure 12 (c) and (d) show timing and performance curves for the Hartman flow test case. It is seen that the time taken by the LU-SGS method is not very different from the global matrix method. This is due to larger number of iterations required by LU-SGS method for steady state convergence. The strong scaling curve in Fig 12(d) indicates better performance for the LU-SGS method.

Capillary discharge simulations

The plume of the capillary discharge is studied using the MHD model. The plasma in the plume of the capillary is nominally of low conductivity and therefore the induced magnetic fields are negligible. The gas dynamics of the plume with thermal conduction, radiation and viscous effects is studied on a geometry shown in Fig 13(a). The capillary is assumed to have a diameter of 2.5 cm. The plate is assumed to have a thickness of 7 mm and is placed at a distance of 4 cm from the capillary exit. Boundary A represents the inlet boundary where a time varying total pressure and temperature is assumed based on the power

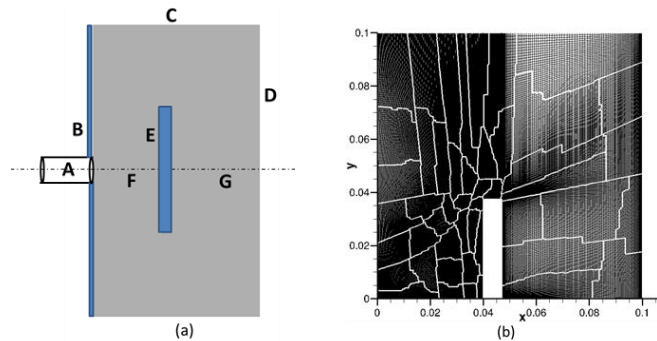


Figure 13: (a) schematic of capillary discharge exit (b) computational mesh with 112,500 cells partitioned among 48 processors.

input to the capillary. The variation of inlet total pressure is shown in Fig 14(a). A peak total temperature of 1.3 eV is assumed at the inlet. This estimate is based on capillary discharge simulations performed by Doyle et al. Boundaries B and E are viscous fixed temperature walls at 300 K and 1000 K respectively. C and D are outflow boundaries where atmospheric pressure is imposed. A symmetry condition is imposed on axis boundaries, F and G. Figure 13(b) shows the computational mesh consisting of 112,500 cells that represents the top half of the geometry. Axi-symmetric simulation is done on the grid using 48 processors. Figure 14(b) shows the plasma temperature and electron densities at three different times during the pulse. A peak temperature ~ 1.1 eV is seen in the stagnation region. The electron densities are computed based on Saha equilibrium equation and is seen to $\sim 10^{22}$ #/m³. These are consistent with time averaged spectroscopic measurements.

The MHD model developed can be used to simulate high density plasmas in any generic electric propulsion device. The unstructured grid framework used in the code gives us the ability to simulate complex geometries, which are otherwise difficult to model using structured meshes. The new device that is being designed by the experimental team does fall in the regime of MHD with geometry similar to that of the capillary discharge. A unified modeling study can be performed from the interior of the device to the plasma plume formation and help in determining accurate spatial distribution of plasma temperatures and densities.

Atomic-scale modeling of plasma-materials interactions (*Henkelman @ UT-Austin*)

In the first year of our project, an atomic scale model of particle interactions with a material surface was developed in order to quantify physical ablation rates. Ablation yields and rates were determined for surfaces of three different materials: a metal, W, a ceramic, Al₂O₃, and a covalent material, Si. The onset of physical ablation was determined

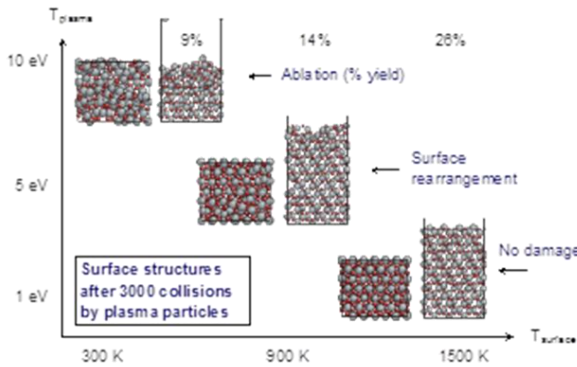


Figure 16: Ablation threshold for alumina as a function of plasma temperature and surface temperature.

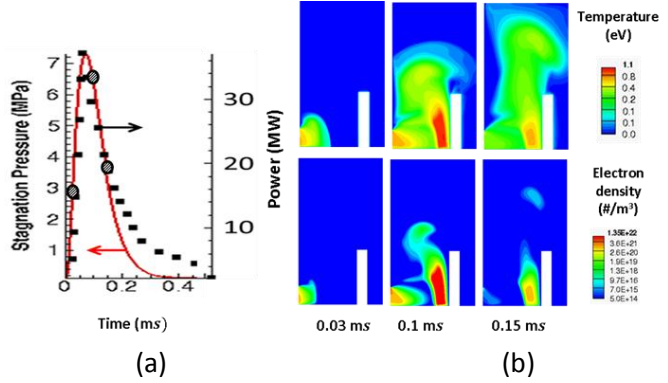


Figure 14: (a) Time varying pressure at the inlet along with experimental power curve (b) Temperature and electron densities at different times.

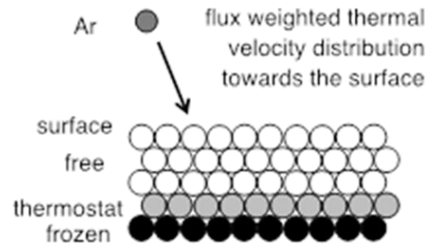


Figure 15: Overview of the MD approach for plasma-materials interactions studies.

in terms of the plasma temperature and the surface temperature. The steady state ablations yields can be integrated over experimental conditions to determine ablation rates for a plasma pulse of known conditions. An analytic model is being developed to allow for the extrapolation of our model in the limit of low exposures to low-temperature and high-density plasma conditions.

The atomic-scale model, shown in the Fig. 15, is based upon molecular dynamics simulations. The surface of a material is represented by a slab of

atoms supported by a frozen layer held in the position of the bulk. A thermostat above this frozen layer is used to remove energy deposited by plasma particles, and to maintain the specified surface temperature. After thermalization, a plasma particle with a velocity drawn from a Maxwell distribution is placed above the surface. Molecular dynamics of the collision is then simulated to determine the response of the surface. The dynamics are integrated for tens of picoseconds until the material has rethermalized, and thermally activated processes on the surface have occurred. Under typical experimental conditions, the collision rate to a nanometer patch of surface is on the order of nanoseconds, so it is appropriate to model collisions as independent events. Many thousands of such collisions are modeled to determine steady-state geometries of the surface, and ablation yields (defined as the ratio of ablated surface atoms to incident plasma atoms).

An example of the results obtained is shown in Fig. 16, for Al_2O_3 . For low plasma temperatures of ~ 1 eV, there is not enough energy in an Ar plasma to have an effect on the surface. Above 5 eV, the plasma atoms have enough energy to roughen the surface, but only at 10 eV is there enough energy to ablate surface atoms. The ablation yield is weakly dependent upon the surface temperature; rougher surfaces at higher temperatures lead to higher ablation yields.

This direct approach to modeling the response of the material works very well at high plasma temperatures (>10 eV) where the probability of an ablation event is high enough to quantify in the thousands of collision events that we can afford to model sequentially.

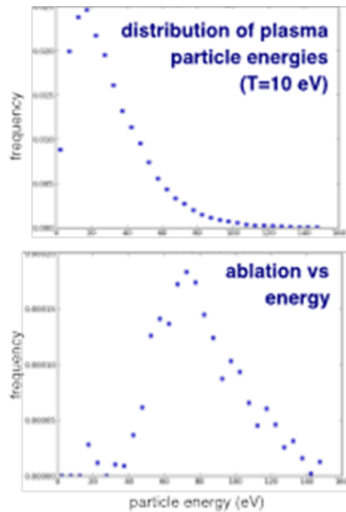


Figure 18: Particle distribution and ablation yield as a function of particle energy for a 10 eV plasma.

Remarkably (see Fig. 19), the extrapolation from a characteristic material response function calculated at 15 eV predicts the same ablation yield when renormalized for a plasma temperature of 10 eV as a direct simulation at for a plasma temperature of 10 eV. This is an encouraging result which suggests that we can use this approach to consider even lower temperature plasmas and lower ablation rates.

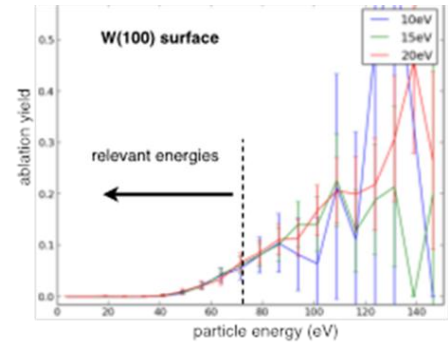


Figure 17: Average ablation yields for single argon particle collisions on silicon.

Such high energies, however, are not characteristic of the experimental plasma conditions. Spectroscopic measurements of the plasma indicate temperatures closer to 1 eV, where ablation yields will be on the order of 1 in a million or less.

To model very low ablation rates, a different kind of analysis is required. The Fig. 17 shows that the average ablation yields due to a single argon particle collisions is very sensitive to the energy of the plasma particle (x-axis), but not to the temperature of the plasma (indicated by the different colors). This means that we can scan over plasma particle energies to generate a characteristic response function of the material. At low energies, a lot of simulation time is required to accurately quantify the ablation yield, but fortunately, this only needs to be done once for each material surface.

With the characteristic material response calculated, and the distribution of plasma particles known (for a given temperature; $T=10$ eV is shown in the Fig. 18), the product of these two functions gives the ablation yield as a function of energy. The integral of this is the average ablation yield for the plasma temperature.

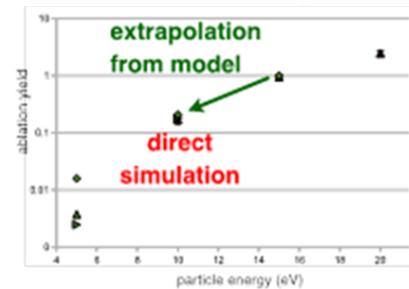


Figure 19: Ablation yield vs. particle energy calculation from direct simulation and model extrapolation.

As well as extrapolating to lower plasma temperatures, future experiments and modeling will explore conditions where higher ablation rates are expected, including materials which are easier to ablate, such as graphite, as well as higher surface temperature and chemically reactive gasses in the plasma. This, combined with atomic scale characterization of the surface using SEM and AFM, will allow for a quantitative comparison of the materials model with the observed material response under experimental plasma conditions.

Interactions, Accomplishments, and Findings

A continuous interaction between all of the team members has been critical to realizing goals of this project. The entire team meets every Friday to discuss progress and exchange information/insights into the research problem at hand. Regular conference calls are held between a subgroup at UT-Austin with the UIUC team to discuss materials related issues. The entire team has benefitted immensely from these interactions. Team members with plasma and pulsed power engineering expertise are gaining an increasing appreciation for material characterization and plasma-materials interactions problems. Materials science experts are gaining a good understanding of plasma related topics. One of the important goals of this program (to foster interactions between multidisciplinary groups) is being realized.

We have made significant progress in our scientific understanding of the plasma-materials interactions in high-pressure, high-power pulsed thermal plasmas. We have developed, improved, and honed the skills, tools and techniques that are being used in this project. Specific accomplishments include:

- 1) The identification of shortcomings of pulsed ablative capillary plasma sources for plasma-materials interactions studies. The post-pulse condensable materials in ablative sources are a dominant source of depositing materials on exposed surfaces, which obfuscates our understanding of the plasma-materials interactions. A new gas-fed, non-ablative, capillary plasma source without need for a fuse-wire ignition scheme has been designed and is being optimized for our studies. The new source will allow the introduction of chemically reactive species that will enhance etch (ablation) processes. Example, small amounts of halogens (that are commonly found in ablative liners of capillary discharges) can be introduced to study chemical etching enhancement to the physical sputter process studied so far. Fast imaging, plasma spectroscopy and other diagnostic tools are being used to characterize this new source.
- 2) Materials characterization techniques such as SEM, GA-XRD, surface profilometry, and EDXS are being used to study samples that have been exposed to our plasma sources. These studies have confirmed the shortcoming of our ablative capillary plasma source. The problems identified by the materials studies include the fact that no detectable material removal (ablation) has been observed for single pulse high-pressure thermal plasma interactions with surfaces. Moreover, the ablative capillary source was found to deposit significant amounts of carbon on the exposed surfaces. Importantly, these studies are beginning to inform us of the types of materials and surfaces that need to be considered for our future studies.
- 3) The plasma source models have been used to simulate the capillary source jet characteristics and the interactions of jets with the exposed materials surfaces. These models have provided very good insights into the dynamics of the transient plasma jet and are in excellent agreement with several experimental measurements. A new computational approach is being developed for low-storage, parallel computing of MHD problems in general. The approach is based on LU-SGS technique specialized for MHD simulations.
- 4) The MD atomistic modeling technique has been used to simulate physical sputtering (ablation) of several materials exposed to inert particle impact, to mimic the plasma-materials interaction experiments we have studied. The MD simulations have clearly demonstrated the very low ablation yields that are achieved under the high-pressure pulsed capillary plasma conditions. These results confirm finding from the materials characterization. A new approach is being developed that will assist in the MD modeling of very low-yield ablation processes. Furthermore the MD model will be enhanced to include chemical etch phenomena in addition to the physical sputter process.